Journal of Superconductivity and Novel Magnetism (2018) 31:2603–2615
https://doi.org/10.1007/s10948-017-4501-y

ORIGINAL PAPER

Structural, Optical, and Magnetic Properties of Nd-Doped CeO_2 Nanoparticles Codoped with Transition Metal Elements (Cu, Zn, Cr)

R. Niruban Bharathi[1] · **S. Sankar**[1]

Received: 4 November 2017 / Accepted: 28 November 2017 / Published online: 16 December 2017

Abstract

In the present work, pure CeO_2, neodymium-doped CeO_2, and neodymium and transition metal element (Cu, Zn, Cr)-codoped CeO_2 nanoparticles were synthesized by an auto-combustion method and annealed at 700 °C. The X-ray diffraction (XRD) studies revealed that all the samples exhibited a single-phase cubic fluorite structure with the incorporation of respective dopant ions into the CeO_2 lattice. The scanning electron microscopy (SEM) images displayed the prepared nanoparticles which had an irregular flaky structure with large agglomerations. The Fourier transform Raman (FT-Raman) spectroscopy analysis revealed the increased oxygen vacancy defects in CeO_2 host after doping and codoping with neodymium and transition metal elements. Ultraviolet-diffuse reflectance spectroscopy (UV-DRS) studies revealed the decrease in bandgap values in doped and codoped samples compared to pure CeO_2 sample. The Fourier transform infrared spectroscopy (FTIR) studies revealed the presence of functional groups in the prepared samples. Photoluminescence (PL) spectroscopy analysis reported the decreased luminescence intensities of Nd-doped and neodymium and transition metal-codoped CeO_2 nanoparticles. The vibrating sample magnetometer (VSM) results depicted that all the samples exhibited room-temperature ferromagnetism.

Keywords Cerium oxide · FT-Raman studies · Oxygen vacancy defects · Room-temperature ferromagnetism

1 Introduction

In the past few decades, nanosized material has received considerable interest due to their optical, electrical, thermal, and magnetic properties as compared to their bulk counter parts. Room-temperature ferromagnetism in transition metal (TM)-doped oxide semiconductors has been reported frequently due to their novel magnetic, magneto-optical, and magneto-electrical properties [1, 2]. These materials are called as oxide-based dilute magnetic semiconductors (O-DMSs) and have led to the intense research in the field of spintronics and magneto-optic applications [3–5].

Dietl et al. [1] theoretically predicated room-temperature ferromagnetism (RTFM) in Mn-doped ZnO. This work was followed by Matsumoto et al. [5], in discovery of room-temperature ferromagnetism in another O-DMSs, Co-doped TiO_2. Since this time, many efforts have been made to detect RTFM in doped transition metal oxides such as ZnO, TiO_2, In_2O_3, and SnO_2 [6–10]. Among these O-DMSs, transition metal and/or rare-earth element-doped cerium oxide materials are considered to be a promising material to realize spintronics devices for many reasons [11, 12]. Cerium oxide is one of the most reactive materials in the lanthanide group which has a cubic fluorite structure in which each cerium site is surrounded by eight oxygen sites in face-centered cubic (FCC) arrangement and each oxygen has a tetrahedron cerium site [13–15]. In addition, CeO_2 nanoparticles have been widely employed in multifunctional applications such as catalysis [16], oxygen sensors [17], solid electrolytes [18], and ultraviolet radiation detectors [19]. Furthermore, cerium oxide has the ability to maintain its fluorite structure when doped with transition

✉ R. Niruban Bharathi
nirubanphd@gmail.com

[1] Condensed Matter Laboratory, Department of Physics, Madras Institute of Technology Campus, Anna University, Chennai, Tamil Nadu, 600044, India

metals or rare-earth elements. Especially, cerium oxide has the structural properties which are very similar to silicon; hence, it can be integrated with conventional silicon-based microelectronic devices [20].

Several studies on magnetic behavior of transition metal-doped CeO_2 nanoparticles and a few studies on rare-earth (RE) element-doped cerium oxide nanoparticles have been reported earlier. Alla et al. [21] showed ferromagnetism at room temperature in Fe-doped CeO_2 nanorods with the highest saturation magnetization of 0.80 Am^{-4}/kg. In another report, Fazal Abbas et al. [22] observed RTFM in Co-doped CeO_2 nanoparticles with the augmentation of saturation values (M_S) that increases with dopant concentration. Dimri et al. [23] reported room-temperature ferromagnetism with rare-earth element (Sm and Nd)-doped CeO_2 nanoparticles prepared by a chemical solution method. Swatsitang et al. [24] showed RTFM in Sm^{3+}doped CeO_2 nanoparticles with the highest saturation magnetization of 0.012 emu/g of a dopant concentration of 15 mol%.

In recent years, transition metals and rare-earth element-codoped cerium oxide nanoparticles were found to express stupendous ferromagnetism at room temperature. For example, Song et al. [25] noticed RTFM when Y^{3+} and Co^{2+} ions were codoped with CeO_2 nanoparticles. Avinash Kumar et al. [26] exposed a ferromagnetic behavior at room temperature when CeO_2 nanoparticles were codoped Eu^{3+} and Fe^{3+} ions. These edicts emphasize that the decent room-temperature ferromagnetic behavior can be expected from CeO_2 nanoparticles codoped with rare-earth ions (Nd) and transition metal elements (Cu, Zn, Cr).

Many methods have been applied to produce doped cerium oxide nanoparticles such as solidstate reaction method [27], chemical precipitation method [28], hydrothermal method [29], Pechini-type sol-gel method [30] and solvothermal method [31]. Among these methods, the citrate-nitrate auto-combustion method has advantages over the other methods mentioned above [32]. In this type of combustion technique, the concept of propellant chemistry is exploited that utilizes the exothermicity of the redox reaction, which takes places between the oxidizer and the fuel [33]. In this citrate-nitrate combustion method, citrate and metal nitrates act as a fuel and oxidizer respectively. Moreover, the combustion technique is convenient, low in cost and simple process for producing a highly pure, homogenous compound with a large surface area of ultrafine nanoparticles.

Therefore, in this report, we have investigated the chance of embellishment of ferromagnetic behavior of transition metal (Cu, Zn, Cr)-doped $Ce_{0.95}Nd_{0.05}O_2$ nanoparticles. The structural, morphological and optical properties were characterized by XRD, SEM, ultraviolet-diffuse reflectance spectroscopy (UV-DRS), Fourier transform infrared spectroscopy (FTIR), Fourier transform Raman (FT-Raman) spectroscopy and photoluminescence (PL) spectroscopy. The magnetic behaviors of samples were studied by vibrating sample magnetometer.

2 Experiment

2.1 Materials

Analytical grades of powders were purchased from all source chemicals: ceric(III) nitrate hexahydrate (Loba Chemie, 99.9%), neodymium(III) hexahydrate (Alfa Aesar, 99.9%), cupric(II) nitrate (Loba Chemie, 99.9%), zinc(II) nitrate (Fisher Chemicals, 99.9%), chromium(III) nitrate (Alfa Aesar, 99.9%) and citric acid anhydrous ($C_6H_7O_8$, 99.9%). Distilled water was used to prepare nanoparticles.

2.2 Synthesis

Pure CeO_2, neodymium doped CeO_2 ($Ce_{0.95}Nd_{0.05}O_2$) neodymium and transition metal-codoped CeO_2 ($Ce_{0.90}Nd_{0.05}Cu_{0.05}O_2$, $Ce_{0.90}Nd_{0.05}Zn_{0.05}O_2$, and $Ce_{0.90}Nd_{0.05}Cr_{0.05}O_2$) nanoparticles were prepared by a citrate-nitrate auto-combustion method. An appropriate amount (as per the stoichiometry) of nitrates and citric acid was dissolved in a beaker containing 20 ml of distilled water. The metal nitrates act as an oxidizer, and citric acid works as a fuel for this combustion reaction. Fuel-to-metal nitrate molar ratio was determined from the concept of propellant chemistry [33]. The resultant mixtures were kept on a hot plate under constant stirring for 2 h at 60 °C. On dehydration of an excess amount of water, the mixtures turned into a colorless viscous gel. The obtained gel was transferred to electric mantle which was kept preheated at 100 °C. After a period of time, gel underwent a vigorous self-propagating combustion reaction to produce yellow porous solid foam of nanoparticles. During the process of combustion reaction, a huge amount of non-toxic gas like N_2, CO_2, and other gaseous products was released as a by-product in the form of brown color fumes. The prepared nanoparticles were annealed at 700 °C for 4 h and ground smoothly for 1 h and used for further characterization. Hereafter, the pure CeO_2, $Ce_{0.90}Nd_{0.05}O_2$, $Ce_{0.90}Nd_{0.05}Cu_{0.05}O_2$, $Ce_{0.90}Nd_{0.05}Zn_{0.05}O_2$, and $Ce_{0.90}Nd_{0.05}Cr_{0.05}O_2$ samples were labeled as CeO_2, CN, CNCu, CNZn, and CNCr, respectively.

2.3 Characterization

The structure and phase identification of prepared nanoparticles was examined by using a Bruker D8 Advance X-ray

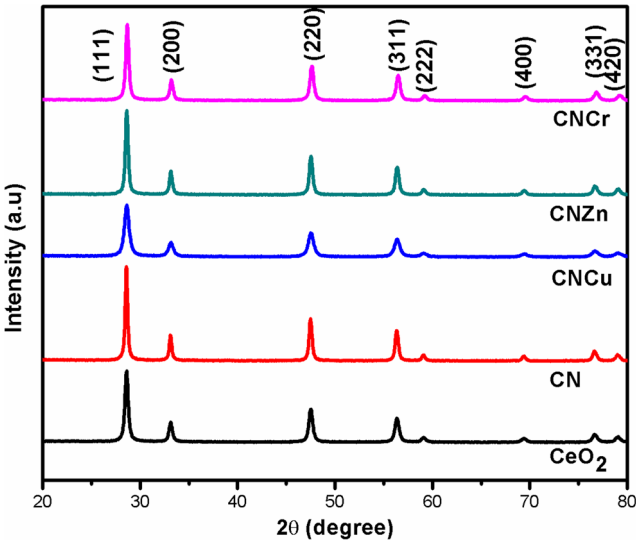

Fig. 1 X-ray diffraction patterns of CeO_2, CN, CNCu, CNZn, and CNCr nanoparticles

diffractometer with Cu-Kα radiation ($\lambda = 1.54056$ Å). The surface morphology, size, and structure of the samples were investigated using Carl Zeiss Supra 55 field emission scanning electron microscopy (FESEM) equipped with Oxford energy-dispersive X-ray spectroscopy (EDS) attachment for elemental analysis. The phonon modes of pure, doped, and codoped CeO_2 nanoparticles were determined by using a Bruker RFS 127 FT-Raman spectrometer. The optical behaviors of all the nanoparticles were studied by using PerkinElmer Lambda 25 UV-DRS spectroscopy. The functional groups present in the prepared nanoparticles were evaluated using a PerkinElmer FT infrared spectrometer. Room-temperature photoluminescence spectra were determined by using a JY Fluorolog-3 spectrofluorometer (PL). The magnetic performance of pure, doped, and codoped CeO_2 nanoparticles was calculated using a Lakeshore 7410 vibrating sample magnetometer (VSM).

3 Results and Discussion

3.1 XRD Studies

The X-ray diffraction pattern was employed to study the crystal structure and phase purity of the prepared nanoparticles. The XRD patterns of CeO_2, CN, CNCu, CNZn, and CNCr nanoparticles are shown in Fig. 1. All the XRD peaks positioned in each sample correspond to (111), (200), (220), (311), (222), (400), (331), and (420) planes that were indexed to cubic fluorite structure with the space group of Fm3m and well matched with the JCPDS card no. 81-0792. No traces of secondary peaks or impurity peaks corresponding to oxide phases of Nd, Cu, Zn, and Cr were observed in the diffraction pattern, indicating that dopants were well incorporated into the CeO_2 lattice site. Moreover, it has been found that the prominent diffraction peak (111) shifts towards lower diffraction angle on doping of Nd ions, whereas on codoping of Nd + TM ions, the prominent peak (111) shifts towards the higher diffraction angle. This behavior reaffirms that dopant ions were successfully incorporated in the CeO_2 lattice structure [34].

From the XRD analysis, the mean crystallite sizes of all the samples were determined using the Scherrer formula [35].

$$D = \frac{0.9\lambda}{\beta \cos\theta} \tag{1}$$

where λ is the wavelength of the X-ray (1.5406 Å), β is the full width at half maximum (FWHM) in radians, and θ is the diffraction angle.

The average crystallite size of CeO_2 nanoparticles was found to be 19.20, which was comparable with the previous report of 20 nm [36]. It can be observed from Table 1 that the crystallite size of CeO_2 nanoparticles increased when doped with Nd ions, and when codoped with Nd + TM ions, the crystallite size decreased. This variance in

Table 1 Structural parameters and bandgap values of CeO_2, CN, CNCu, CNZn, and CNCr nanoparticles

Sample name	Average crystallite size (D; nm)		Lattice constant ($a = b = c$; Å)	Lattice strain (ε; $\times 10^{-3}$	Dislocation density (δ; line/m^2 $\times 10^{-15}$)	Volume (V; Å)	Bandgap (E_g; eV)
	From Scherrer	From the W-H plot					
CeO_2	19.20	17.20	5.4011	4.08	2.7116	157.56	3.25
CN	26.24	20.55	5.4042	3.245	1.4514	157.83	3.21
CNCu	13.71	12.69	5.3974	5.495	5.3154	157.23	2.90
CNZn	22.65	20.08	5.3969	3.505	1.9478	157.2	3.19
CNCr	20.30	17.82	5.3878	3.945	2.4250	157.40	2.95

crystallite size on doping and codoping can be attributed to the incorporation of Nd^{3+} and TM ions (Cu^{2+}, Zn^{2+}, Cr^{2+}) in the CeO_2 crystal lattice sites. Figure 2a clearly shows the variation on crystallite size as a function of dopants in the CeO_2 nanoparticles. In general, the codoping of Nd + TM ions in CeO_2 lattice induces structural defects specifically oxygen vacancies in the grain boundaries and in the lattice sites that in turn causes densification that restricts the grain growth which reduces the crystallite size of the samples [37].

The lattices constant a of the prepared samples was deconvoluted using the following relations [38]:

$$\frac{1}{d_{hkl}} = \left(\frac{h^2 + k^2 + l^2}{a^2}\right)_{(a=b=c)} \quad (2)$$

where d_{hkl} is the interplanar spacing and h, k, and l are the corresponding Miller indices to each line in the XRD pattern.

The lattice constant values of CeO_2, CN, CNCu, CNZn, and CNCr nanoparticles were calculated and are listed in Table 1. The calculated lattice constant value of CeO_2 nanoparticles was found to be 0.54011 nm which was less than that of the bulk CeO_2 (0.5411 nm). It is clear that the lattice constant increases with the addition of Nd ions in the CeO_2 lattice. After codoping of Nd + TM ions, there is a linear decreasing trend in lattice constant values as shown in Table 1. This variation in lattice constant can be attributed due to the difference in the ionic radii of host Ce^{4+} (0.97 Å) being replaced by dopants with the ionic radii of Nd^{3+} (0.983 Å), Cu^{2+} (0.57 Å), Zn^{3+} (0.88 Å), and Cr^{2+} (0.64 Å) ions [39–42]. Figure 2b illustrates the variation

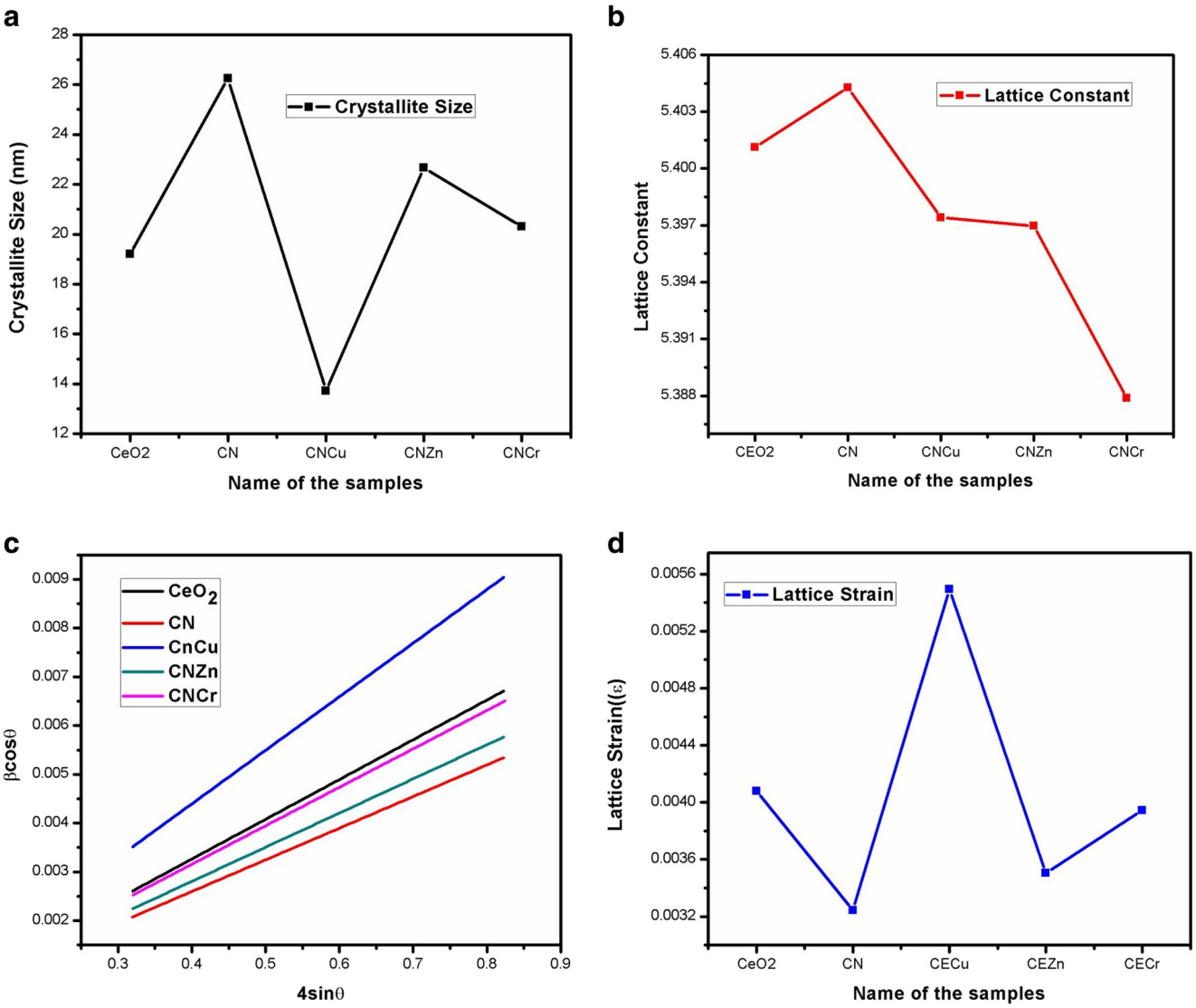

Fig. 2 **a** Variation of crystallite size with various dopants of CeO_2 nanoparticles. **b** Variation of lattice constant with various dopants of CeO_2 nanoparticles. **c** W-H plot of CeO_2, CN, CNCu, CNZn, and CNCr nanoparticles. **d** Variation of lattice strain with various dopants of CeO_2 nanoparticles

of lattice constant with respect to the various dopants of CeO_2. Moreover, it is observed from the XRD pattern that the intensity of the diffraction peak (111) of CeO_2 increases with width enhancement when codoped with neodymium and transition metal ions. This behavior was related to the strain associated with lattice constants.

The lattice strain value associated with the crystallite size variation of each sample can be calculated using the Williamson-Hall (W-H) method [43]. The W-H equation is given by

$$\beta \cos\theta = \frac{0.9\lambda}{D} 4\eta \sin\theta \tag{3}$$

where β is the FWHM, θ is the diffraction angle, λ is the wavelength of the X-ray, D is the crystallite size of the sample and η is the lattice strain. A plot was drawn between $4\sin\theta$ (x-axis) against $\beta\cos\theta$ (y-axis) for all reflections shown in Fig. 2c. The slope and the y-intercept of the linear fitted line represent the lattice strain and crystallite size respectively. The lattice strain values and crystallite sizes are listed in Table 1.

It is apparent from Table 1 that the strain value increases when codoped with Nd + TM ions when compared with CeO_2 nanoparticles. In the CeO_2 sample, lattice strain originated due to the oxygen vacancy defects and Ce^{3+} ions present in the surface of the structure [43]. In codoped samples, the lattice strain values are enhanced due to the formation of more oxygen vacancies (V_O) in the structure to maintain the charge neutrality [44]. Figure 2d displays the increase in the lattice strain values as a function of dopants in the CeO_2 samples. Noteworthy, the mean crystallite size from both the Scherrer and W-H methods was in good agreement. In addition, these strains could be localized at the subgrain and subdomain levels near grain boundaries,

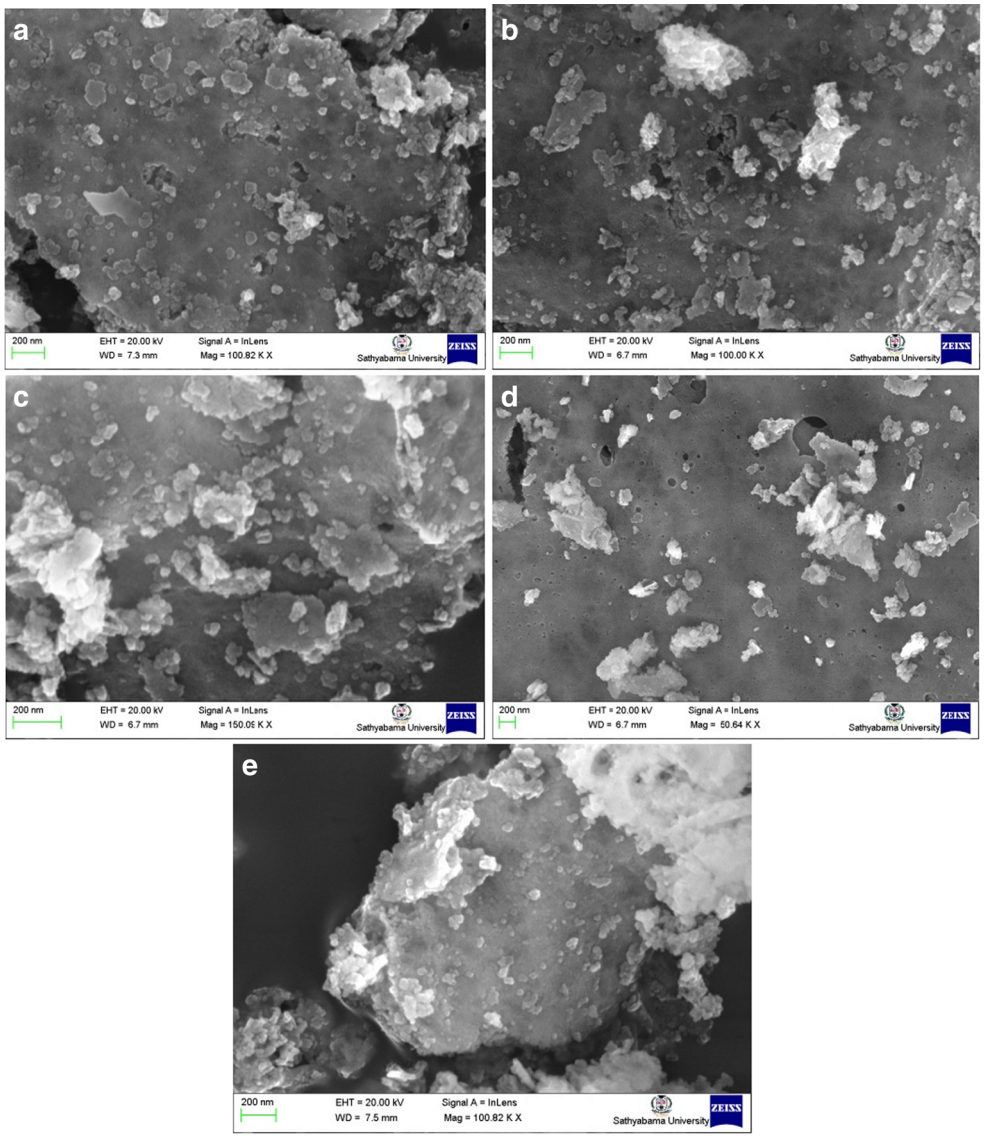

Fig. 3 FESEM micrograph of **a** CeO_2, **b** CN, **c** CNCu, **d** CNZn, and **e** CNCr nanoparticles

which may also be a reason for the reduction of the crystallite size in doped and codoped samples [45].

3.2 Morphological Studies

The field emission scanning electron microscopy study was carried out to examine the surface morphologies of the prepared samples. Figure 3a-e displays the FESEM images of CeO_2, CN, CNCu, CNZn, and CNCr nanoparticles prepared by a combustion method. All the nanoparticles were formed as a foam type exhibiting a porous nature with aggregated particles. It can be seen from the images that all the nanoparticles show a flaky and platelet structure with large aggregates. These sorts of porous nature of nanoparticles were usually observed in combustion reaction due to the evaporation of a large amount of unwanted gases in the reaction mixture during combustion. Moreover, doping of neodymium ions and codoping of neodymium and transition metal ions in CeO_2 do not influence the morphologies of the samples. Figure 4a-e shows the energy-dispersive X-ray spectra of all the nanoparticles which confirm the presence of respective dopant ions in the CeO_2 composition.

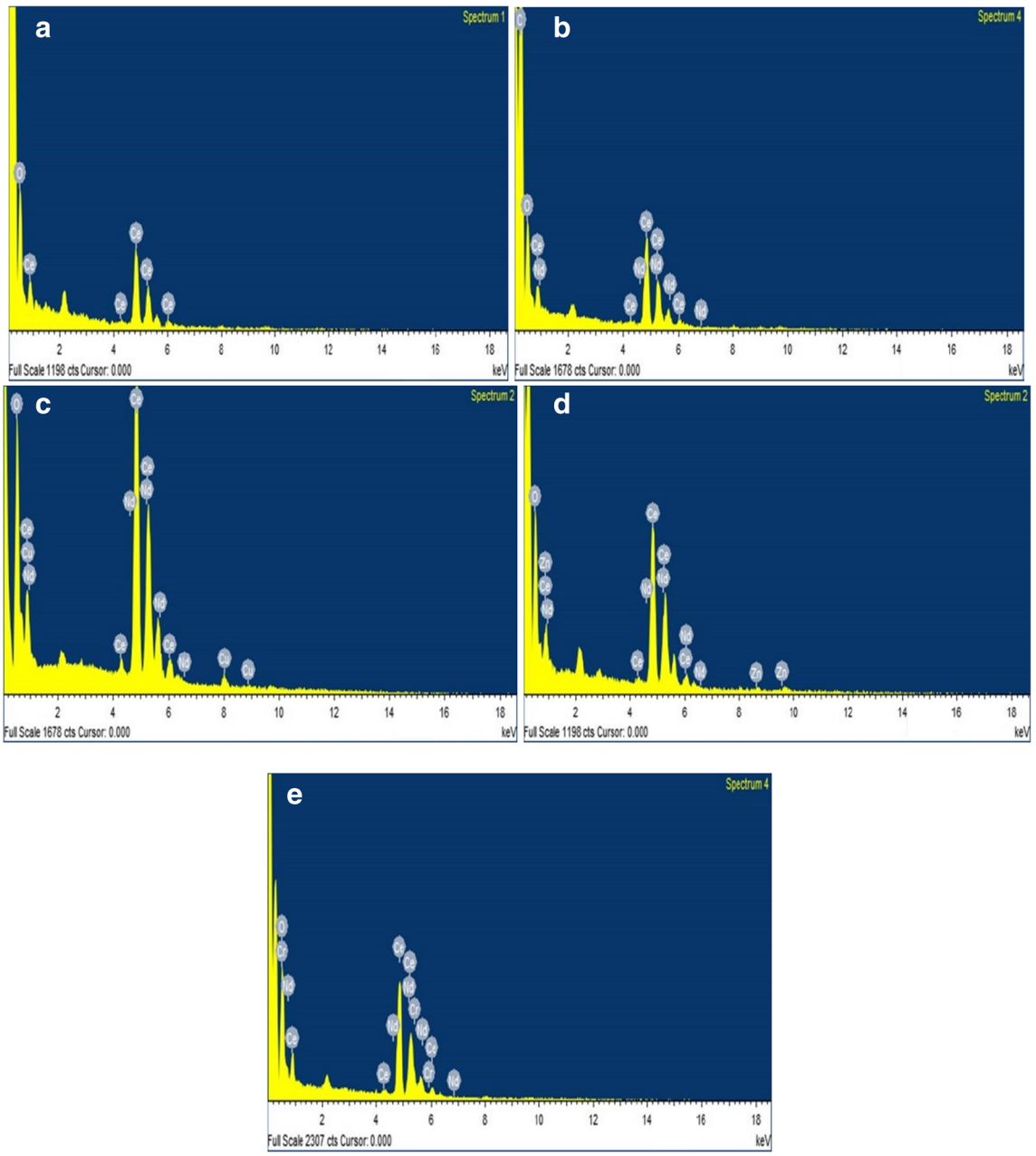

Fig. 4 EDS spectrum of **a** CeO_2, **b** CN, **c** CNCu, **d** CNZn, and **e** CNCr nanoparticles

3.3 FT-Raman Studies

FT-Raman spectral analysis of the prepared nanoparticles was carried out to confirm the phase chastity and metal-oxygen bond arrangements. FT-Raman spectra of CeO_2, CN, CNCu, CNZn, and CNCr nanoparticles are shown in Fig. 5. The high intense band centered at 464 cm^{-1} is denoted as the triple-degenerated F_{2g} Raman active mode of the cubic fluorite structure of CeO_2 [46]. This first-order F_{2g} Raman active mode can be ascribed to the rhythmic stretching (phonon) mode oxygen anion around each Ce^{4+} cation. Since only the oxygen atoms move, the vibrational mode is roughly independent to the cation mass [47]. It is clear from the spectra that the F_{2g} active peak shifted towards a lower wavelength when CeO_2 nanoparticles were doped with neodymium ions. This shift is attributed to the origination of oxygen vacancies in the fluorite structure to maintain the charge neutrality in the structure [48]. Codoping with neodymium and transition metal ions on CeO_2 lattice, the F_{2g} Raman band shifts further towards the lower frequencies due to the formation of a large amount of oxygen vacancies in the structure. Furthermore, the peak intensity of F_{2g} Raman active mode gets quelled when doped and codoped with Nd + TM ions. This suppression was often associated with the formation of crystal structure with plenty of oxygen defects as a result of dopant-induced effects [49].

3.4 UV-DRS Studies

To derive the bandgap information of prepared nanoparticles, UV-diffuse reflectance studies were carried out in the range of 200–1400 nm. The UV-DRS spectra of CeO_2, CN, CNCu, CNZn, and CNCr nanoparticles are shown in Fig. 6. From the DRS spectra, the optical absorption coefficient can be determined using the Kubelka-Munk function [50].

$$F(R) = \frac{(1-R)^2}{2R} \tag{4}$$

where R is the diffuse reflectance. The Kubelka-Munk plot of all the samples is shown in the inset of Fig. 6. It is apparent from the spectra that the absorption threshold edge of CeO_2 nanoparticles is observed at 260 nm. The absorption edge of Nd-doped and Nd + TM-codoped CeO_2 nanoparticles gets red shifted (below 400 nm) relative to that of CeO_2 nanoparticles. These ultraviolet absorption edges are due to the electronic transition from the $2p$ valence band of O^{2-} to the $4f$ band of Ce^{4+} [51]. The red shift of the absorption edges of doped and codoped CeO_2 samples could be due to the result of interfacial polaron effect arising from the electron-phonon interaction [52].

For the evaluation of bandgap, $[F(R)h\vartheta]^{1/2}$ is plotted against energy and the straight part of the curve was extrapolated to zero [50] and this gives the bandgap values of all the samples as shown in Fig. 7a-e. The obtained bandgap value of CeO_2 nanoparticles was found to be 3.25 eV, which agreed well with the values of previous reports [53]. The bandgap value decreased on doping with Nd ions and decreased more on codoping with Nd + TM ions as shown in Table 1. The introduction of Nd and TM ions in the CeO_2 lattice creates a ground and excited energy states on the mid band of CeO_2 as explained in the absorption spectra. These energy states trap many excited electrons

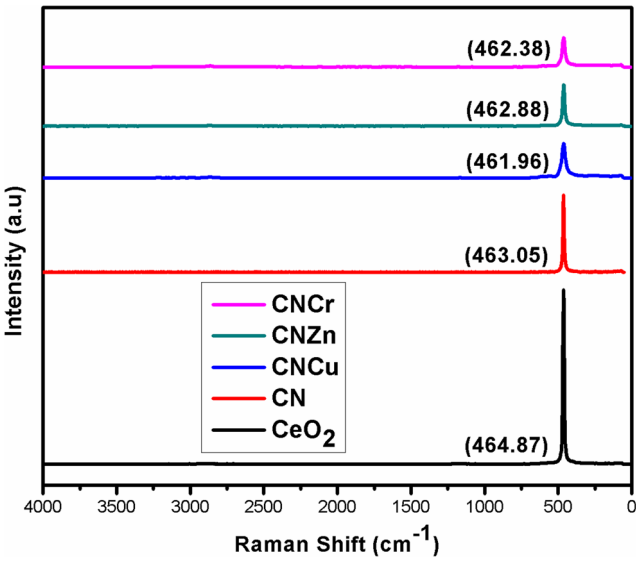

Fig. 5 Raman spectra of CeO_2, CN, CNCu, CNZn, and CNCr nanoparticles

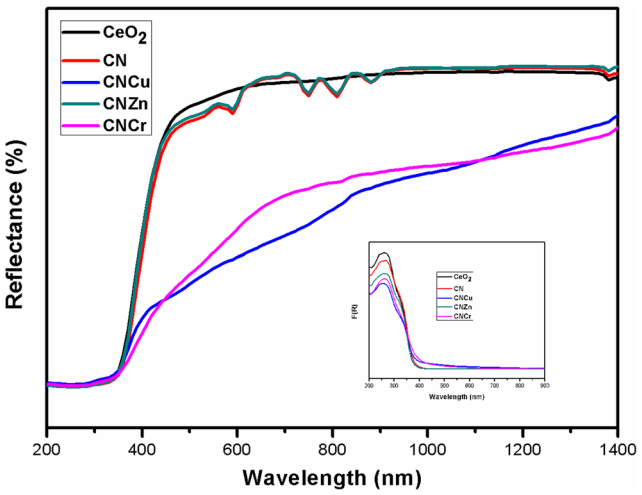

Fig. 6 UV-DRS spectra of CeO_2, CN, CNCu, CNZn, and CNCr nanoparticles. Inset, Kubelka-Munk versus wavelength of CeO_2, CN, CNCu, CNZn, and CNCr nanoparticles

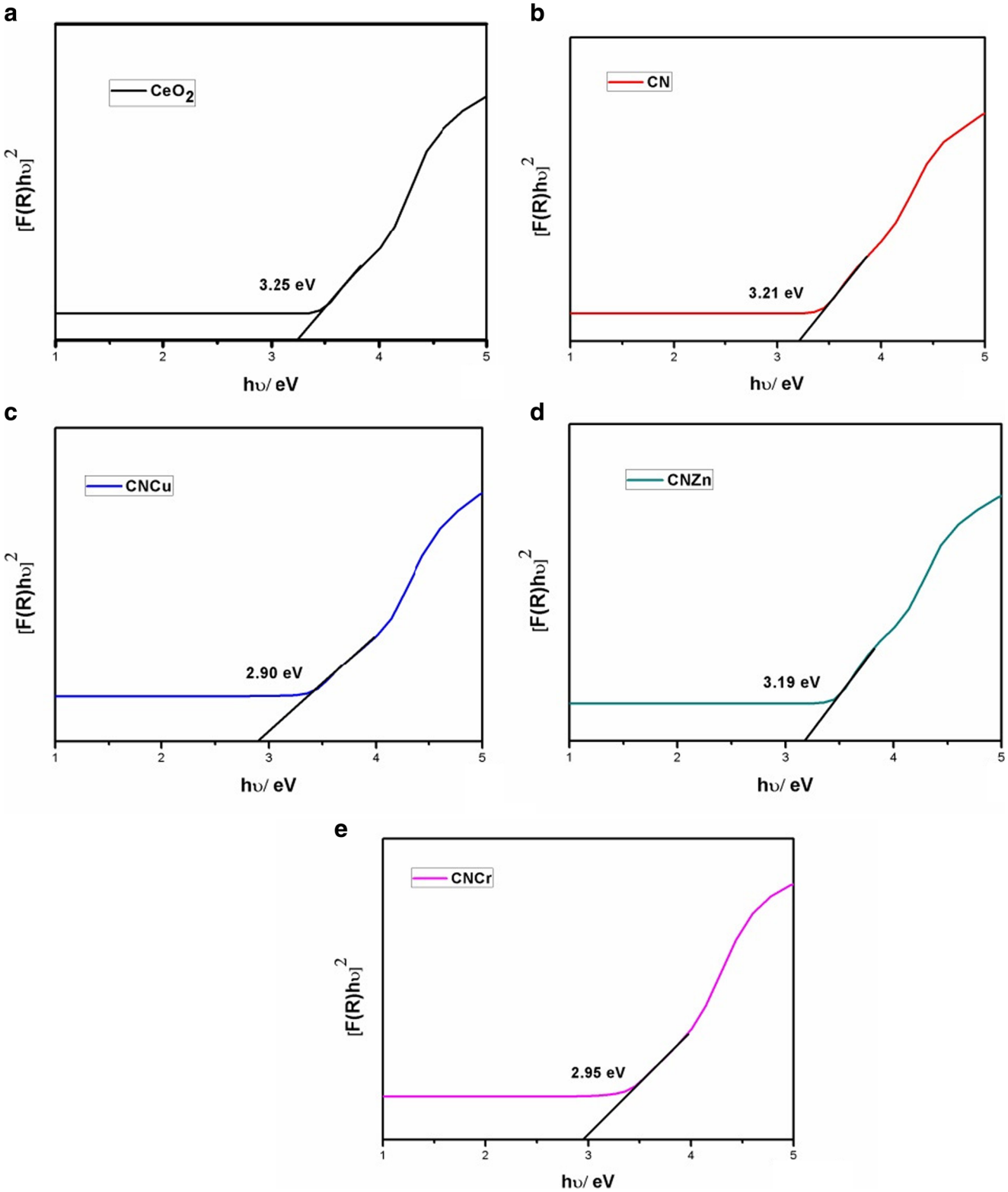

Fig. 7 Bandgap of **a** CeO_2, **b** CN, **c** CNCu, **d** CNZn, and **e** CNCr nanoparticles

coming from the O^{2-} $2p$ level. This phenomenon causes the reduction in the bandgap on doping and codoping. In addition, the observed decrease in bandgap on doping and codoping could be due to the variation in the microstructural parameter such as crystallite size and lattice constant [54] as listed in Table 1.

3.5 FTIR Studies

The position of functional groups and the nature of chemical bonding in the prepared nanoparticles were investigated using an FTIR technique. FTIR transmission spectra of CeO_2, CN, CNCu, CNZn, and CNCr nanoparticles at room temperature in the frequency range of 400–4000 cm^{-1} are shown in Fig. 8. The strong intense bands observed at 3458 cm^{-1} of all the samples can be attributed to O–H vibration modes of H-bonded water molecules, which was due to the physically observed water on the samples [55, 56]. The absorption bands centered at 2985 cm^{-1} correspond to the C–H stretching vibrations. The two intense bands at 1578 and 1420 cm^{-1} correspond to the stretching vibration of carboxylate salts (COO^-) [57]. The weak bands centered at 1012 cm^{-1} were ascribed to the cerium-oxygen groups with a larger double-bond character [58]. The strong bands observed at 554 cm^{-1} are due to the symmetrical stretching vibration mode of (Ce-O-Ce) or (Ce-O-Nd) or (Ce-O-TM), indicating the Nd ions and transition metal ion-doped ceria nanoparticles [59]. In addition, these bands get shifted towards higher frequencies when CeO_2 nanoparticles were doped and codoped with Nd + TM ions, and this confirms the incorporation of dopants into the CeO_2 structure [60].

3.6 Photoluminescence Studies

Photoluminescence analysis is a promising technique to find out the defects in the structures. Figure 9 depicts the room-temperature photoluminescence spectra of CeO_2, CN, CNCu, CNZn, and CNCr nanoparticles at an excitation wavelength of 270 nm. It can be seen from the spectra that CeO_2 nanoparticles consist of six peaks centered on 422, 442, 453, 470, 483, and 493 nm in the region between 400 and 525 nm. Nd-doped and Nd + TM-codoped CeO_2 nanoparticles exhibit an analogous type of emission bands as that of CeO_2 nanoparticles. All samples exhibit three blue emission peaks located at 422, 442, and 453 nm and three blue-green emission peaks centered at 470, 483, and 493 nm with the varied intensities. In general, the emission bands positioned between 350 and 540 nm are ascribed to the existence of structural defects including oxygen vacancies which were formed between Ce^{4+} conduction band and O^{2-} valence band [61–63]. In view of Gnanam et al. [64] and Huang et al. [65], the emission bands centered from 370 and 440 nm can be attributed to excitonic recombination in the near-band edge (NBE) emission of CeO_2. In another report by Meng et al. [66], there were wide emission bands from 445 to 550 nm which can be ascribed to the transition from the level of different defects to the O $2p$ band. The emission band observed at 422 nm is due to the charge transfer between Ce $4f$ conduction states to O $2p$ valence band [67]. According to Wang et al. [68], an emission band located at 470 nm is due to the abundant defects such as dislocation which was helpful for the fast oxygen transportation. With regard to the emission band that appeared around 482 nm, Kwok et al. [69] reported that it is due to the transition from the level of the ionized oxygen vacancies to the valence band.

Moreover, the PL intensities of the Nd-doped and Nd + TM-codoped CeO_2 nanoparticles get decreased compared with CeO_2 nanoparticles. On doping and codoping of Nd and transition metal ions, luminescence intensity decreased which is due to the formation of oxygen vacancy defects in the structure. Codoping of Nd + TM ions in the CeO_2 samples exhibited very low emission intensities, thereby

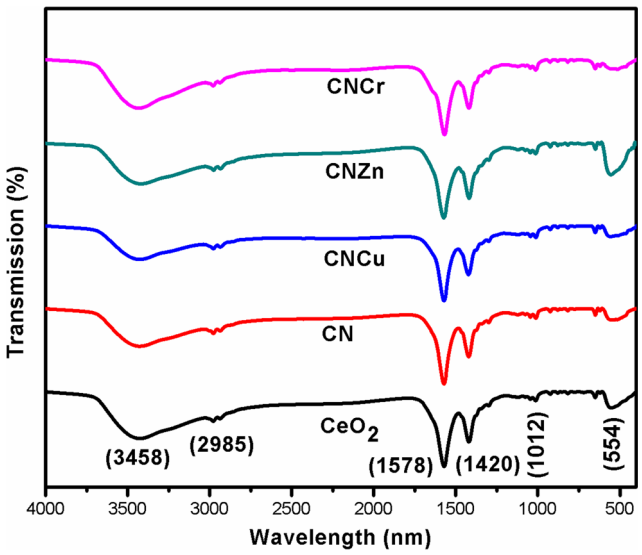

Fig. 8 FTIR spectra of CeO_2, CN, CNCu, CNZn, and CNCr nanoparticles

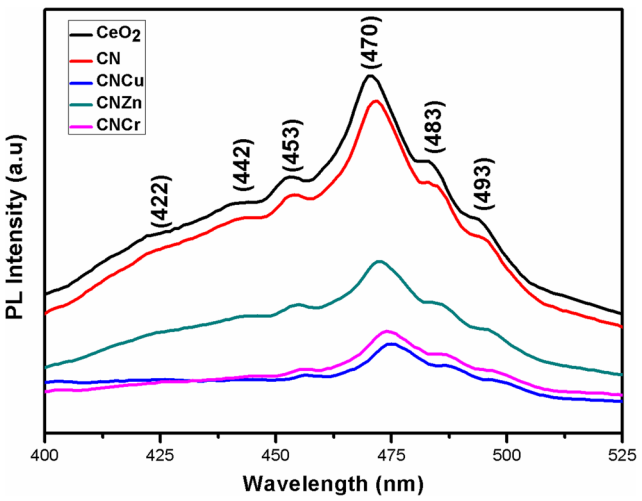

Fig. 9 Photoluminescence spectra of CeO_2, CN, CNCu, CNZn, and CNCr nanoparticles

indicating the generation of relatively high density of non-radioactive oxygen vacancy defects in the structure [61] as elucidated in XRD and FT-Raman studies.

On comparison with CeO_2 nanoparticles, the emission peaks of doped and codoped CeO_2 samples were found to be red shifted. This red shift is due to the formation of oxygen defects and the conductive conditions for Ce^{3+} formation [43]. These defect states from Ce^{3+} states were localized slightly below the Ce $4f$ conduction band. Furthermore, these red shifts of emission peak of Nd-doped and Nd + TM-codoped CeO_2 samples may be also due to the bandgap normalization effect (BRG) [70].

3.7 Magnetic Studies

To explore the magnetic properties of CeO_2, CN, CNCu, CNZn, and CNCr nanoparticles at room temperature, vibrating sample magnetometer measurement has been performed under the applied magnetic field in the ± 15 kOe. The room-temperature M-H curve of all the samples is shown in Fig. 10. It can be seen from the graph that all the samples exhibit ferromagnetism in room-temperature. Magnetic parameters such as saturation magnetization (M_S), remanent magnetization (M_R), and coercivity (H_C) were calculated, and the values are listed in Table 2.

It is apparent from the graph that pure CeO_2 nanoparticles exhibited weak ferromagnetism at room temperature though bulk CeO_2 shows to be diamagnetic in nature. This FM behavior has been already reported in earlier studies. For example, Sundaresan et al. [71] observed room-temperature ferromagnetism in undoped CeO_2 nanoparticles and explained the origin of ferromagnetism through the exchange interaction between the electron spin moments originated from the oxygen vacancies present at the surface of the particles. Coey et al. [72] noticed RTFM in CeO_2 nanoparticles and depicted the origin of ferromagnetism in undoped CeO_2 through an F-centered mechanism. According to this mechanism, a considerable amount of oxygen vacancies and Ce^{3+} ions was present in the CeO_2 nanoparticles. These oxygen vacancy defects can induce local magnetic moment in the nearby Ce^{3+} ions. These Ce^{3+} ions have an electronic configuration of partially filled $4f$ orbital with one unpaired electron. Thus, an exchange interaction between the Ce^{3+} and electron bond to oxygen vacancies (i.e., Ce^{3+}-V_O-Ce^{3+}) led to the ferromagnetic behavior in CeO_2 nanoparticles. From the M-H graph, it was observed that all samples exhibited room-temperature ferromagnetism with the increase in saturation values. The substitution of Nd ions in CeO_2 lattice can systematically inflate the number of oxygen vacancies in the

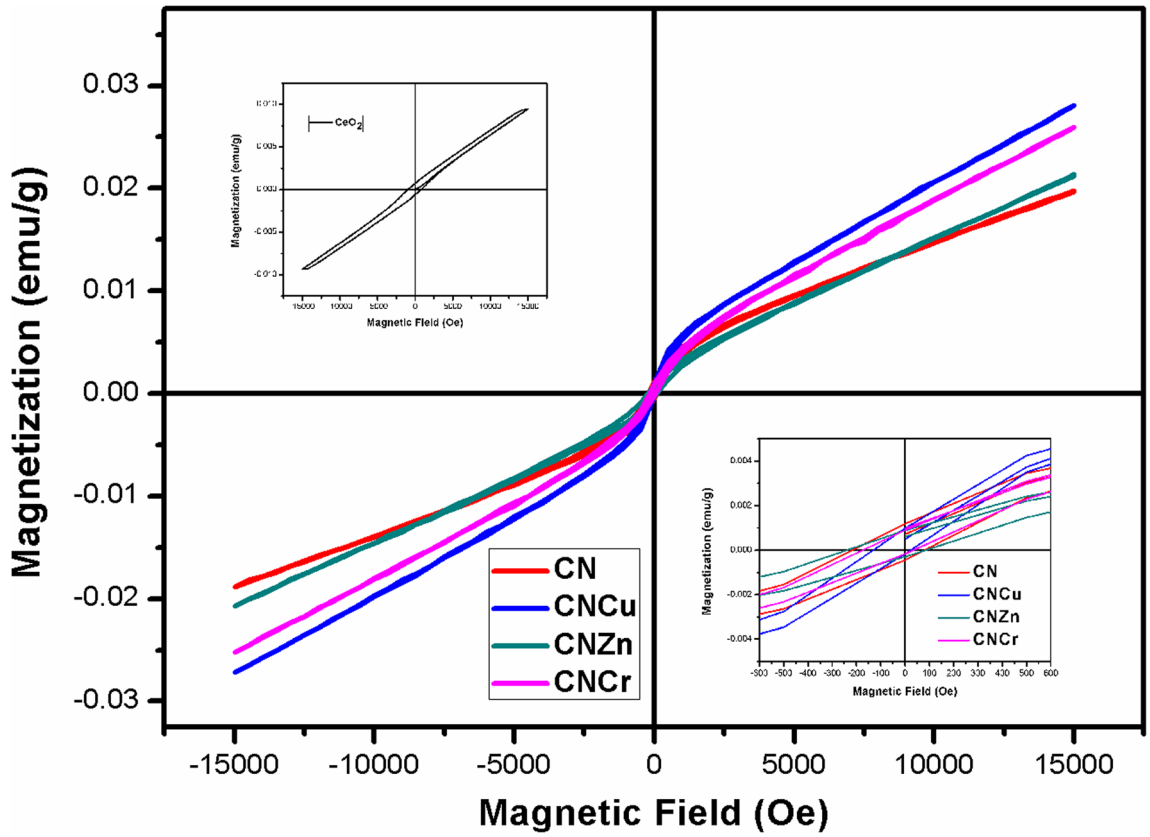

Fig. 10 M-H loops of CN, CNCu, CNZn, and CNCr nanoparticles (left inset). M-H loops of CeO_2 nanoparticles (right inset), showing the magnified M-H loops of CN, CNCu, CNZn, and CNCr nanoparticles

Table 2 Magnetic parameters of CeO_2, CN, CNCu, CNZn, and CNCr nanoparticles

Sample name	Saturation magnetization (M_S) (emu/g) $\times 10^{-2}$	Remanent magnetization (M_R) (emu/g) $\times 10^{-2}$	Coercivity (H_C; Oe)	Squareness ratio (SQR)
CeO_2	0.9389	0.06634	890.99	0.07065
CN	1.9295	0.08176	148.46	0.04237
CNCu	2.7692	0.05796	77.397	0.03176
CNZn	2.1037	0.05983	162.81	0.02844
CNCr	2.5601	0.05337	104.35	0.02084

system relative to that of CeO_2 nanoparticles. This increase in V_O, in turn, caused the increase in the Ce^{3+}-V_O-Ce^{3+} complexes, resulting in the augmentation of saturation magnetization. The FM behavior of codoped CeO_2 samples at room temperature can be described on the basis of the ferromagnetic exchange coupling of F centers which were involved with oxygen vacancies and transition metal ions. Codoping of Nd + TM ions in the CeO_2 host lattice promotes the origination of oxygen vacancies to maintain the charge neutrality. An oxygen vacancy in the CeO_2 can trap an electron to form an F center. This oxygen vacancy can establish groups with two magnetic ions, i.e., TM-V_O-TM or Ce^{3+}-V_O-TM complexes in this case. Moreover, electron trapped by the oxygen vacancy occupies an orbital which overlaps the shells of neighboring polarons. From the concepts of Hund's rule and the Pauli exclusion principle, an electron trapped in the oxygen vacancy should possess spin in the direction parallel to the neighboring polarons. Thus, the overlapping of such neighboring polarons offers long-range ferromagnetic ordering in codoped CeO_2 nanoparticles. Hence, the observed RT ferromagnetism in CNCu, CNZn, and CNCr samples can be ascribed to the occurrence of magnetic ions mediated by the oxygen vacancies [72–74].

The saturation magnetization value of CeO_2 nanoparticles was found to be 9.38×10^{-3} emu/g which was comparable with the previous studies [22]. The M_S values of Nd-doped and Nd + TM-codoped CeO_2 nanoparticles were found to increase as enlisted in Table 2. This increase is due to the formation oxygen vacancy defects and charge carriers produced by the defects in the host lattice.

The remanent magnetization (M_R) values of all the prepared nanoparticles were acquired from M-H loops and are listed in Table 2. From the table, the M_R values of Nd-doped CeO_2 samples were found to increase when compared with the CeO_2 nanoparticles. The increase in M_R values is attributed to the increase in the saturation magnetization values of Nd-doped CeO_2 samples.

The quality of the samples was examined by squareness ratio (SQR). The squareness ratio was estimated using the following relation [75]:

$$\mathrm{SQR} = \frac{M_R}{M_S} \tag{5}$$

The SQR values ranging from 0.05755 to 0.02084 with doped and codoped CeO_2 nanoparticles are enlisted in Table 2. These values are less than 0.5 for all the samples which reveal that all the nanoparticles possess uniaxial anisotropy produced through internal strains [76].

4 Conclusion

Through a simple citrate-nitrate auto-combustion method, pure CeO_2, Nd-doped CeO_2, and Nd + TM-codoped CeO_2 nanoparticles were prepared. The structural, optical, and magnetic properties were studied. The formations of cubic fluorite structure of all the samples were confirmed by XRD studies. Surface morphologies of the prepared nanoparticles had a flaky and porous nature with irregular shape analyzed through SEM. The presence of respective dopants in the CeO_2 host was confirmed by EDS spectra. An increase in oxygen vacancies in doped and codoped CeO_2 samples was analyzed by FT-Raman and FTIR studies. The blue-green emission peaks obtained at 470 nm in PL spectra proved the presence of oxygen vacancy defects in all the samples. The VSM studies revealed that the saturation magnetization values of doped and codoped CeO_2 nanoparticles got increased compared to CeO_2 nanoparticles.

References

1. Dietl, T., Ohno, H., Matsukura, F., Cibert, J., Ferrand, D.: Zener model description of ferromagnetism in zinc-blende magnetic semiconductors. Science **287**, 1019–1022 (2000)
2. Pearton, S.J., Heo, W.H., Ivill, M., Norton, D.P.: Dilute magnetic semiconducting oxides, semiconductor. Sci. Technol. **19**, R59–R74 (2004)
3. Wolf, S.A., Awschalom, D.D., Buhrmam, R.A., Daughton, J.M., Von Molnar, S., Roukes, M.L., Chtchel Kanova, A.Y., Treger, D.M.: Spintronics: a spin-based electronics vision for the future. Science **294**, 1488 (2001)
4. Ohno, H.: Making nonmagnetic semiconductors ferromagnetic. Science **281**, 951 (1998)
5. Matsumoto, Y., Murakami, M., Shono, T., Hasegawa, T., Fukumura, T., Kawasaki, M.: Room-temperature ferromagnetism in transparent transition metal-doped titanium dioxide. Science **291**, 854–856 (2001)
6. Abbas, F., Jan, T., Iqbal, J., Sajjad, M., Naqvi, H.: Fe doping induced enhancement in room temperature ferromagnetism and

selective cytotoxicity of CeO_2 nanoparticles. Curr. Appl. Phys. **15**, 1428–1434 (2015)
7. Krithiga, R., Sankar, S., Arunkumar, V.: F-center-mediated ferromagnetic ordering in K-doped ZnO. J. Supercond. Novel Magn. **29**, 245–251 (2016)
8. Rajamanickam, N., Kanmani, S.S., Rajashabala, S., Ramachandran, K.: Influence of Sr doping on structural, optical and magnetic properties of TiO_2 nanoparticles. Mater. Lett. **161**, 520–522 (2015)
9. Sai Krishna, N., Kaleemulla, S., Amarendra, G., Madhusudhana Rao, N., Krishnamoorthi, C., Kuppan, M., Rigana Begam, M., Sreekantha Reddy, D., Omkarame, I.: Structural, optical, and magnetic properties of Fe doped In_2O_3 powders. Mater. Res. Bullet. **61**, 486–491 (2015)
10. (Dorneanu), P.P., Airinei, A., Grigoras, M., Fifere, N., Sacarescu, L., Lupu, N., Stoleriu, L.: Structural, optical and magnetic properties of Ni doped SnO_2 nanoparticles. J. Alloys Compd. **668**, 65–72 (2016)
11. Yang, S., Zhang, Y.: Structural and magnetic properties of Cr- and Fe-doped CeO_2 nanoparticles prepared by sol-gel method. Mater. Sci. Forum **848**, 682–687 (2016)
12. Paunovic, N., Dohcevic-Mitrovic, Z., Scurtu, R., Askrabic, S., Prekajski, M., Matovic, B., Popovic, Z.V.: Suppression of inherent ferromagnetism in Pr-doped CeO_2 nanocrystals. Nanoscale **4**, 5469 (2012)
13. Tarnuzzer, R.W., Colon, J., Patil, S., Seal, S.: Vacancy engineered ceria nanostructures for protection from radiation-induced cellular damage. Nano Lett. **5**, 2573–2577 (2005)
14. Park, E.-J., Choi, J., Park, Y.-K., Park, K.: Oxidative stress induced by cerium oxide nanoparticles in cultured BEAS-2B cells. Toxicology **245**, 90–100 (2008)
15. Chen, P.-L., Chen, I.-W.: Reactive cerium (IV) oxide powders by the homogeneous precipitation method. J. Amer. Ceram. Soc. **76**, 1577–1583 (1993)
16. Valenzuela, R.X., Bueno, G., Solbes, A., Sapina, F., Martínez, E., Corberan, V.C.: Nanostructured ceria-based catalysts for oxydehydrogenation of ethane with CO_2. Top. Catal. **15**, 2–4 (2001)
17. Ramamoorthy, R., Akbar, S.A., Dutta, P.K.: Dependence of potentiometric oxygen sensing characteristics on the nature of electrodes. Sens. Actuators B **113**, 162–168 (2006)
18. Hormesa, J., Pantelouris, M., Balazs, G.B., Rambabu, B.: X-ray absorption near edge structure (XANES) measurements of ceria-based solid electrolytes. Solid State Ionics **136–137**, 945–954 (2000)
19. Morimoto, T., Tomonaga, H., Mitani, A.: Ultraviolet ray absorbing coatings on glass for automobiles. Thin Solid Films **351**, 61–65 (1999)
20. Tiwari, A., Bhosle, M., Ramachandran, S., Narayan, N.S.J., Gupta, B.A.: Ferromagnetism in Co doped CeO_2, observation of a giant magnetic moment with a high Curie temperature. Appl. Phys. Lett. **88**, 142511–142513 (2006)
21. Alla, S.K., Devarakonda, K.K., Komarala, E.V.P., Mandal, R.K., Prasad, N.K.: Ferromagnetic Fe-substituted cerium oxide nanorods: synthesis and characterization. Mater. Des. **114**, 584–590 (2017)
22. Abbas, F., Iqbal, J., Jan, T., Sajjad, M., Naqvi, H., Gul, A., Abbasi, R., Mahmood, A., Ahmad, I., Ismail, M.: Differential cytotoxicity of ferromagnetic Co doped CeO_2 nanoparticles against neuroblastoma cancer cells. J. Alloys Compd. **648**, 1060–1066 (2015)
23. Dimri, M.C., Khanduri, H., Kooskora, H., Subbi, J., Heinmaa, I., Mere, A., Krustok, J., Stern, R.: Ferromagnetism in rare earth doped cerium oxide bulk samples. Phys. Status Solidi (A) **209**, 353–358 (2012)
24. Swatsitang, E., Phokha, S., Hunpratub, S., Maensiri, S.: Characterization of Sm-doped CeO_2 nanoparticles and their magnetic properties. Physica B **485**, 14–20 (2016)
25. Yuan-Qiang, S., Huai-Wu, Z., Qi-Ye, W., Hao, Z., Xiao, J.Q.: Additional Y^{3+} doping effect on ferromagnetism of $Ce_{0.97}Co_{0.03}O_{2-\delta}$ compounds. Chin. Phys. Lett. **25**, 1106–1109 (2008)
26. Avinash Kumar, R., Suresh Babu, K., Dasgupta, A., Ramaseshan, R.: Enhancing the dual magnetic and optical properties of Co-doped cerium oxide nanostructures. RSC Adv. **5**, 103465–103473 (2015)
27. Liu, X., Chen, S., Wang, X.: Synthesis and photoluminescence of CeO_2:Eu^{3+} phosphor powders. J. Lumin. **127**, 650–654 (2007)
28. Cho, J.-H., Bass, M., Babu, S., Dowding, J.M., Self, W.T., Seal, S.: Up conversion luminescence of Yb^{3+}-Er^{3+} Co doped CeO_2 nanocrystals with imaging applications. J. Lumin. **132**, 743–749 (2012)
29. Wang, L., Menga, F., Li, K., Lu, F.: Characterization and optical properties of pole-like nano-CeO_2 synthesized by a facile hydrothermal method. Appl. Surf. Sci. **286**, 269–274 (2013)
30. Guo, H.: Green and red upconversion luminescence in CeO_2:Er^{3+} powders produced by 785nm laser. J. Solid State Chem. **180**, 127–131 (2007)
31. Al-Agel, F.A., Al-Arfaj, E., Al-Ghamdi, A.A., Losovyj, Y., Bronstein, L.M., Mahmoud, W.E.: A novel recipe to improve the magnetic properties of Mn doped CeO_2 as a room temperature ferromagnetic diluted metal oxide. J. Magn. Magn. Mater. **360**, 73–79 (2014)
32. Suan, M.S.M., Johan, M.R., Siang, T.C.: Synthesis of $Y_3Ba_5Cu_8O_{18}$ superconductor powder by auto-combustion reaction: effects of citrate–nitrate ratio. Physica C **480**, 75–78 (2012)
33. Jain, S.R., Adiga, K.C.: A new approach to thermochemical calculations of condensed fuel-oxide. Combust. Flame **40**, 71–79 (1981)
34. Liyanage, A.D., Perera, S.D., Tan, K., Chabal, Y., Balkus, K.J. Jr.: Synthesis, characterization and photocatalytic activity of Y-doped CeO_2 nanorods. ACS Catal. **4**, 577–584 (2014)
35. Hassanzadeh-Tabrizia, S.A., Mazaheri, M., Aminzare, M., Sadrnezhaad, S.K.: Reverse precipitation synthesis and characterization of CeO_2 nanopowder. J. Alloys Compd. **491**, 499–502 (2010)
36. Jahagirdar, A.A., Zulfiqar Ahmed, M.N., Donappa, N., Nagabhushana, H., Nagabhushana, B.M.: Cod removal of an industrial effluent using nan crystalline ceria synthesized by solution combustion method. J. Appl. Chem. **1**, 14–17 (2012)
37. Patsalas, P., Logothetidis, S., Sygellou, L., Kennou, S.: Structure-dependent electronic properties of nanocrystalline cerium oxide films. Phys. Rev. B; Condens. Matter Phys. **68**, 035104 (2003)
38. Liu, I.-T., Hon, M.-H., Kuan, C.-Y., Teoh, L.-G.: Structure and optical properties of Ag/CeO_2 nanocomposites. Appl. Phys. A **111**, 1181–1186 (2013)
39. Choudhury, B., Borah, B., Choudhury, A.: Ce-Nd codoping effect on the structural and optical of properties of TiO_2 nanoparticles. Mater. Sci. Eng. B **178**, 239–247 (2013)
40. Al-Agel, F.A., Al-Arfaj, E., Al-Ghamdi, A.A., Stein, B.D., Losovyi, Y., Brostien, L.M., Shokr, F.S., Mahmoud, W.E.: Structure and magnetic properties of diluted magnetic metal oxide based on Cu-doped CeO_2 nanopowders. Ceram. Int. **41**, 1115–1119 (2015)
41. Ramasamy, V., Vijayalakshmi, G.: Effect on Zn doping on structural, optical and thermal properties of CeO_2 nanoparticles. Superlattice. Microstruct. **85**, 510–521 (2015)
42. Alla, S.K., Devarakonda, K.K., Komarala, E.V.P., Mandal, R.K., Prasad, N.K.: Structural and optical and magnetic properties of Cr-substituted CeO_2 nanoparticles. Mater. Chem. Phys. **182**, 280–286 (2016)

43. Choudhury, B., Choudhury, A.: Ce^{3+} and oxygen vacancy mediated tuning of structural and optical properties of CeO_2 nanoparticles. Mater. Chem. Phys. **131**, 666–671 (2012)
44. Patil, S., Seal, S.: Role of trivalent La and Nd dopants in lattice distortion and oxygen vacancy generation in cerium oxide nanoparticles. Appl. Phys. Lett. **88**, 243110 (2006)
45. Mir, F.A., Batoo, K.M., Chatterjee, I., Bhat, G.M.: Preparation and Ac electrical characterizations of Cd doped SnO_2 nanoparticles. J. Mater. Sci. Mater. Electron. **25**, 1564–1570 (2014)
46. Zawadzki, M.: Preparation and characterization of ceria nanoparticles by microwave-assisted solvothermal process. J. Alloys Compd. **454**, 347–351 (2008)
47. Suzuki, T., Kosacki, I., Anderson, H.U.: Electrical conductivity and lattice defects in nanocrystalline cerium oxide thin films. J. Amer. Ceram. Soc. **84**, 2007–2014 (2001)
48. Kostic, R., Askrabic, S., Mitrovic, Z.D., Popovic, Z.V.: Low-frequency Raman scattering from CeO_2 nanoparticles. Appl. Phys. A: Mater. Sci. Process. **90**, 679–683 (2008)
49. Araujo, V.D., Avansi, W., de Carvalho, H.B., Moreira, M.L., Longo, E., Ribeiro, C., Bernardi, M.I.B.: CeO_2 nanoparticles synthesized by a microwave-assisted hydrothermal method: evolution from nanospheres to nanorods. Cryst. Eng. Commun. **14**, 1150–1154 (2012)
50. Elavarthi, P., Kumar, A.A., Murali, G., Amaranatha Reddyand, D., Gunasekhar, K.R.: Room temperature ferromagnetism and white light emissive Cds:Cr nanoparticles synthesized by chemical co-precipitation method. J. Alloys Compd. **656**, 510–517 (2016)
51. Manoharan, D., Vishista, K.: Optical properties of nano-crystalline cerium dioxide synthesized by single step aqueous citrate-nitrate gel combustion method. Asian J. Chem. **25**, 9045–9049 (2013)
52. Amarsingh Bhabu, K., Theerthagiri, J., Madhavan, J., Balu, T., Muralidharan, G., Rajasekaran, T.R.: Cubic fluorite phase of samarium doped cerium oxide $(CeO_2)_{0.96}Sm_{0.04}$ for solid oxide fuel cell electrolyte. J. Mater. Sci. Mater. Electron. **27**, 1566–1577 (2015)
53. Sababri Arul, N., Mangalaraj, D., In Han, J.: Facial hydrothermal synthesis of CeO_2 nanoparticles. Bullet. Mater. Sci. **38**, 1135–1139 (2015)
54. Abbas, F., Jana, T., Iqbala, J., Ahmad, I., Sajjad, M., Naqvi, H., Malikd, M.: Facile synthesis of ferromagnetic Ni doped CeO_2 nanoparticles with enhanced anticancer activity. Appl. Surf. Sci. **357**, 931–936 (2015)
55. Samiee, S., Goharshadi, E.K.: Effects of different precursors on size and optical properties of ceria nanoparticles prepared by microwave-assisted method. Mater. Res. Bullet. **47**, 1089–1095 (2012)
56. Wang, G., Mu, Q., Chen, T., Wang, Y.: Synthesis, characterization and photoluminescence of CeO_2 nanoparticles by a facile method at room temperature. J. Alloys Compd. **493**, 202–207 (2010)
57. Yang, Z., Yang, Y., Liang, H., Liu, L.: Hydrothermal synthesis of monodisperse CeO_2 nanocubes. Mater. Lett. **63**, 1774–1777 (2009)
58. Binet, C., Badri, A., Lavalley, J.-C.: A spectroscopic characterization of the reduction of ceria from electronic transitions of intrinsic point defects. J. Phys. Chem. **98**, 6392–6398 (1994)
59. Ho, C., Jimmy, C., Kwong, T., Mak, A.C., Lai, S.: Morphology-controllable synthesis of mesoporous CeO_2 nano and microstructures. Chem. Mater. **17**, 4514–4522 (2005)
60. Tholkappiyan, R., Vishista, K.: Synthesis and characterization of barium zinc ferrite nanoparticles: working electrode for dye sensitized solar cell applications. Solar Energy **106**, 118–128 (2014)
61. Choudhury, B., Choudhurya, A.: Room temperature ferromagnetism in defective TiO_2 nanoparticles: role of surface and grain boundary oxygen vacancies. J. Appl. Phys. **114**, 203906 (2013)
62. Choudhury, B., Chetri, P., Choudhury, A.: Oxygen defects and formation of Ce^{3+} affecting the photocatalytic performance of CeO_2 nanoparticles. RSC Adv. **4**, 4663–4671 (2014)
63. Lei, Y., Zhang, L.D., Meng, G.W., Li, G.H., Zhang, X.Y., Liang, C.H., Chen, W., Wang, S.X.: Preparation and photoluminescence of highly ordered TiO_2 nanowire arrays. Appl. Phys. Lett. **78**, 1125 (2001)
64. Gnanam, S., Rajendran, V.: Synthesis of CeO_2 or A-Mn_2O_3 nanoparticles via sol–gel process and their optical properties. J. Sol-Gel Sci. Technol. **58**, 62–69 (2011)
65. Huang, Y.F., Cai, Y.B., Qiao, D.K., Liu, H.: Morphology-controllable synthesis and characterization of CeO_2 nanocrystals. Particuology **9**, 170–173 (2011)
66. Meng, F.M., Wang, L.N., Cui, J.B.: Controllable synthesis and optical properties of nano-CeO_2 via a facile hydrothermal route. J. Alloys Compd. **556**, 102–108 (2013)
67. Morshed, A.H., Moussa, M.E., Bedair, S.M., Leonard, R., Liu, S.X., El-Masry, N.: Violet/blue emission from epitaxial cerium oxide films on silicon substrates. Appl. Phys. Lett. **70**, 1647 (1997)
68. Wang, G., Mu, Q., Chen, T., Wang, Y.: Synthesis, characterization and photoluminescence of CeO_2 nanoparticles by a facile method at room temperature. J. Alloys Compd. **493**, 202–207 (2010)
69. Kwok, W.M., Djurisic, A.B., Leung, Y.H., Chan, W.K., Phillips, D.L.: Time-resolved photoluminescence from ZnO nanostructures. Appl. Phys. Lett. **87**, 223111 (2005)
70. Duan, J.X., Huang, X.T., Wang, H., Zhong, Q., Sunand, F.L., He, X.: Synthesis of porous ZnO micro-flakes via an integrated autoclave and pyrolysis process. Mater. Chem. Phys. **106**, 181–186 (2007)
71. Sundaresan, A., Bhargavi, R., Rangarajan, N., Siddesh, U., Rao, C.N.R.: Ferromagnetism as a universal feature of nanoparticles of the otherwise nonmagnetic oxides. Phys. Rev. B **74**, 161306 (2006)
72. Coey, J.M.D., Venkatesan, M., Fitzgerald, C.B.: Donor impurity band exchange in dilute ferromagnetic oxides. Nat. Mater. **4**, 173–179 (2005)
73. Wen, Q.-Y., Zhang, H.-W., Song, Y.-Q., Yang, Q.-H., Zhu, H., Xiao, J.Q.: Room-temperature ferromagnetism in pure and co doped CeO_2 powders. J. Phys. Condens. Matter **19**, 246205–246212 (2007)
74. Xia, C., Hu, C., Chen, P., Wan, B., He, X., Tian, Y.: Magnetic properties and photoabsorption of the Mn-doped CeO_2 nanorods. Mater. Res. Bullet. **45**, 794–798 (2010)
75. Topkaya, R., Baykal, A., Demir, A.: Yafet–Kittel-type magnetic order in Zn-substituted cobalt ferrite nanoparticles with uniaxial anisotropy. J. Nanoparticle Res. **15**, 1359 (2013)
76. Ammar, S., Helfen, A., Jouini, N., Fievet, F., Rosenman, I., Villain, F., Molinie, P., Danot, M.: Magnetic properties of ultrafine cobalt ferrite particles synthesized by hydrolysis in a polyol medium. J. Mater. Chem. **11**, 186–192 (2001)